Deposition of Particles on Ocular Tissues and Formation of Krukenberg Spindle, Hyphema, and Hypopyon

Satish Kumar

Sumanta Acharya[1]
Professor
e-mail: acharya@LSU.edu

Department of Mechanical Engineering,
Louisiana State University,
Baton Rouge, LA, 70803

Roger Beuerman
LSU Eye Center,
New Orleans, LA 70112

Eye diseases, such as Krukenberg's spindle, hyphema, and hypopyon, are related to the deposition of specific particles such as pigmentary cells, leukocytes, and erythrocytes. These particles are circulated by the aqueous humor (AH) and tend to deposit in regions of low velocities or high resistance. In the present paper, numerical simulations are reported of the AH flow and particle transport, and the particle concentration predictions are qualitatively compared to clinical images. The particle concentration distributions provide an understanding of the likely sources of deposition and the origin of the deposited particles. Pigmentary cells are seen to concentrate in a vertical band on the corneal surface consistent with clinical observations of Krukenberg's spindle. Leukocytes and erythrocytes are seen to collect at the bottom of the anterior chamber similar to the observations made for hypopyon and hyphema. These results confirm the potential of using numerical calculations in order to obtain a better understanding of the particle transport and deposition patterns in the anterior chamber of the eye.
[DOI: 10.1115/1.2472380]

Introduction

Particles of different sizes, shapes, and traits circulate inside the anterior chamber of the eye. Examples of such particles include pigment particles, protein particles (albumin), erythrocytes, and leukocytes. The interaction of these particles with the ocular tissues depends on their particular characteristics and the aqueous humor (AH) flow field inside the anterior chamber. Deposition of these particles in the different regions of the eye can lead to the obstruction of the aqueous flow, increased intraocular pressure (IOP), and blurred vision. For example, pigment dispersion syndrome (PDS) is a condition with high concentration of pigment granules in the aqueous humor that leads to the pigment deposition on the corneal endothelium in a vertical band known as *Krukenberg's spindle* (KS), or pigment deposition in the trabecular meshwork (TM). The rupture of blood vessels and bleeding inside the eye leads to accumulation of blood (erythrocytes) inside the anterior chamber and the formation of *hyphema*. In cases of ocular inflammation, leukocytes sediment at the bottom of the anterior chamber and form a white layered structure known as *hypopyon*.

Since detailed in situ measurements in the living eye are difficult, there is limited understanding of the mechanisms and the nature of the particle deposition and buildup. This understanding can be useful in developing prevention and remediation strategies. The goal of this paper is to perform computational simulations inside a geometrical model of rabbit eye to get insight about the movement and deposition of particles of different characteristics leading to the formation of clinically observed structures in the eye.

Aqueous humor is secreted in the posterior chamber of eye by the ciliary body and then it enters the anterior chamber through the pupil. The bulk flow rate of the aqueous humor into the anterior chamber of normal human eye varies in the range of 1.5–2.5 μL/min, while for pigmented rabbits it varies in the range of 1.0–2.5 μL/min [1]. More than 80% of the aqueous humor exits through the TM into the Schlemm's canal, which is located in the vicinity of the junction between the iris and cornea. The aqueous humor is then discharged into the venous system, either through the aqueous veins or through the episcleral veins [2]. Another exit pathway for the AH is the uveoscleral drainage system, in which the AH enters the iris root and passes between the muscle bundles in the ciliary body to the choroids and out through the episcleral tissues. This pathway contributes little to the outflow (20%) and is neglected in the present study [3]. Buoyancy is the dominant mechanism driving the fluid flow in the anterior chamber of the eye [4,5]. This was also confirmed in the computational studies by Kumar et al. [6], where calculations were done with buoyancy alone (no inflow through the pupil), buoyancy plus inflow (i.e., with pressure gradient across pupil), and inflow alone (no buoyancy). It was demonstrated that the solutions with buoyancy alone matched well with the solutions with buoyancy plus inflow, indicating that buoyancy played a critical role in the flow transport. The presence of blood vessels inside the iris and ciliary body maintain them at the body temperature (37°C) [7], while the outer layer of the cornea, which is exposed to ambient conditions, is generally maintained at 32–33°C by the tear film evaporation and continuous blinking of eye [8,9]. This small temperature gradient across the anterior chamber plays a major role in controlling the flow field inside the eye.

Intraocular pressure (IOP) is the primary parameter used for the diagnosis of glaucoma-related eye diseases. The blockage of the drainage system of the eye due to the clogging of the TM pores by the particles circulating with the AH can increase the IOP to some abnormal value. The outflow network system of the eye consists of a graded porous mesh from the inside of the eye to the outside. These include (i) the uveal and corneoscleral meshwork, (ii) the juxtacanalicular meshwork (JCM), (iii) the endothelial wall of the Schlemm's canal, (iv) the Schlemm's canal, and (v) the aqueous veins. Both the uveal and corneoscleral meshwork have negligible resistance because of their bigger pore size (25–75 μm) [2]. It is

[1]Corresponding author.
Contributed by the Bioengineering Division of ASME for publication in the JOURNAL OF BIOMECHANICAL ENGINEERING. Manuscript received December 29, 2004; final manuscript received September 5, 2006. Review conducted by Fumihiko Kajiya. Paper presented at the 2004 ASME International Mechanical Engineering Congress (IMECE2004), Anaheim, California, USA, November 13–19, 2004.

believed that the tortuous flow passage from the JCM accounts for the most of the flow resistance [10,11] because of its very small pore size (~0.6–2.0 μm) [12–14] and the presence of the extracellular matrix gel in the open spaces.

Geometrical modeling of the TM is an extremely challenging task, and although efforts have been made to study the role of the TM and Schlemm's canal on the outflow resistance through very idealized models, none of the computational flow simulations (inside the anterior chamber) reported to date [3–5,15–17] have included the TM in their calculations. In the present study, the TM is modeled as an annular two-zone porous gutter with specified pore size in each zone and a void fraction of 0.5 [6].

Scott [15,16] has presented a finite element model for calculating the temperature rise in an eye induced by the exposure to infrared radiation, but the intraocular flow field was not determined in their work. Heys et al. [3] have developed a two-dimensional model of the coupled aqueous humor-iris system for determining the contribution of aqueous humor flow and passive iris deformation to the iris contour shape. Their model predicts the iris contour and the iris-to-lens contact, which is primarily a function of the aqueous flow rate, the permeability of the TM and posterior pathway and iris modulus. Heys and Barocas [4] have extended this work to predict the effects of accommodation on the iris position and the pressure distribution in the anterior chamber. The azimuthal symmetry in these models, the neglect of the gravity and buoyancy effects, and the neglect of the effect of the TM on the pressure distribution, limits the applicability of these models in accurately predicting the flow mechanisms inside the eye.

The two studies reporting flow simulations in the eye, and most relevant to the present work, are those of Canning et al. [5] and Heys and Barocas [17]. Canning et al. [5] solved the flow profile inside the anterior chamber using a simplified three-dimensional computational model and analyzed the deposition of particles leading to the formation of structures inside the eye. Heys and Barocas [17] presented three-dimensional flow simulations but neglected the effect of TM on the transport and deposition of pigment particles. Through experimental observations, the TM is believed to play a major role in the entrapment of particles through its pores [18]. Kumar et al. [6] have presented a three-dimensional model of a rabbit eye, exploring the effect of TM pore size and different orientations of the eye. Predicted pressure drop and shear stress values in [6] agreed well with published results and provided a measure of validation to the computational model. However, the particle transport process has not been studied in [6]. The present paper is perhaps the first one that includes the effect of the TM, models it as a porous meshwork, and examines the effect of the TM on the flow distributions and particle transport. Therefore, unlike earlier studies, no ad hoc boundary conditions are imposed at the inlet to the TM.

A key goal of the present study is to analyze the transport of particles (pigmentary cells, leukocytes, and erythrocytes) and to identify the specific locations where they are likely to deposit. These deposition patterns are linked to the formation of specific structures, such as Krukenberg's spindle, hyphema, and hypopyon, and the potential origin of the deposited particles is explored in this study. The calculations of the flow field and the particle deposition patterns include the TM, which is modeled as a two-zone porous structure with the first zone representing the uveal and corneoscleral meshwork and the second zone representing the juxtacanalicular meshwork. Particle simulations are performed for both the horizontal and vertical (upward-facing) orientation of the eye in order to assess how orientation affects the particle deposition process. The geometric modeling and incorporation of the TM and evaluation of the orientation effects on the particle transport have not been reported earlier.

Particle Characteristics

Pigment Particles. Pigmentary glaucoma and pigment dispersion syndrome (PDS) is a condition found most commonly in young males [19]. This condition is believed to be a consequence of the deposition of pigment particles (melanin granules) on the ocular tissues of the eye. It is believed that rubbing of the peripheral iris with the lens surface or anterior zonular packets cause liberation of melanin granules from the iris [19]. Most of the melanin granules are released from the posterior surface (surface toward the posterior chamber) of the iris and enter into the anterior chamber with the aqueous humor. There is considerable scatter in the documented information about the size, density, and concentration of these particles in the aqueous humor. Its diameter is of the order of 0.5–1 μm [20] and density is ~1700 Kg/m^3 [5]. Kuchle et al. [21] report measurements of approximately 9700 melanin granules of PDS in 250 μL of aqueous humor. These values are used in the present work.

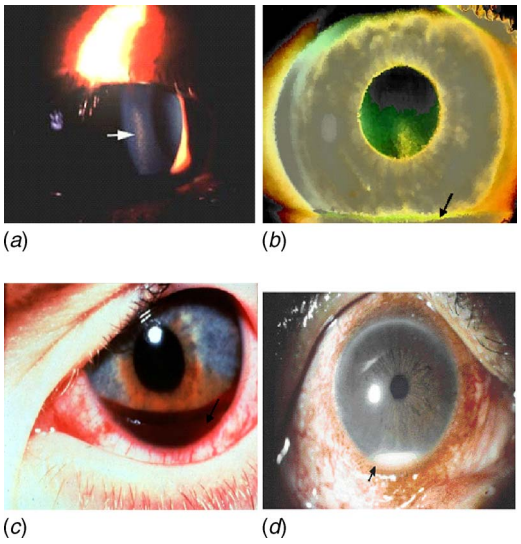

Fig. 1 (*a*) KS as a vertical spindle on the corneal surface [25], (*b*) KS formation due to the accumulation of pigment particles at lower portion of the corneal surface [26], (*c*) a typical hyphema [26], and (*d*) hypopyon (sedimentation of leukocytes at the bottom of the anterior chamber) [26]

These pigment particles have the property of stickiness and can adhere to the posterior part of the cornea leading to the accumulation of particles on the corneal surface in some distinctive shape (Figs. 1(*a*) and 1(*b*)), commonly known as Krukenberg's spindle (KS). It is found that distributions of the pigment granules on the corneal surface are both extra- and intra-endothelial. According to a previous hypothesis of the formation of KS, pigment particles first adhere to the irregularities on the endothelial surface of the cornea and later the granules are phagozytized and accumulated on the endothelial cells that lead to the formation of KS structures [19]. Because of the smaller size and volume of the pigment particles, vision is generally not obstructed by the formation of the smaller KS, but all patients with KS should be considered as glaucoma suspects [22]. As KS structures are an indication of pigment dispersion in the anterior chamber, there are possibilities of clogging of the pores of TM with pigment particles in eyes with KS structures, thereby increasing the IOP [23].

Erythrocytes. Red blood cells or erythrocytes are one of the important constituents of the blood. Under normal conditions, 1 mm^3 of blood contains $4-5\times10^6$ erythrocytes [24]. The diameter of these red blood cells lies in the range of 6.7–7.7 μm and density is ~1000 Kg/m^3 [5]. Ghost cells that are more than 120 days old lose their pliability to get deformed and are much denser than fresh red cells (1500 Kg/m^3) [5]. They take a rigid spherical shape and due to incapability of deformation they tend to get stuck in the TM and clog the drainage system of the eye.

Normally, erythrocytes are not found in the anterior chamber,

but the damage of the intraocular tissues or breakdown of the blood-ocular barrier causes the accumulation of the blood in the anterior chamber. This hemorrhage in the anterior chamber and accumulation of blood in the anterior chamber is a very serious problem commonly referred as hyphema. Tiny hemorrhages are visible in the form of erythrocytes floating and circulating in the aqueous humor. Slightly larger amounts of blood settle as variously shaped masses on the surface of the iris and lens. Still larger hemorrhages gravitate to the inferior aspect of the anterior chamber producing a grossly visible layered hyphema (Fig. 1(*c*)). For the most severe hemorrhages, impaired circulation of AH causes clotting of blood and trabecular blockage with normal sickle erythrocytes. Clotting of the TM increases the resistance to outflow and consequently leads to an increase of IOP, which can go up to 50 mm of Hg in some severe cases of hyphema [27]. Continued bleeding and elevated IOP for a long time may lead to onset of glaucoma, optical atrophy, and sometimes corneal blood staining (in case of total hyphema), which results in final poor vision [28].

One of our objectives is to formulate a model to analyze the sedimentation of erythrocytes in anterior chamber. The sources of bleeding modeled are (i) tear in the anterior face of the ciliary body or disruption in the arterial circle of the iris [27] and (ii) blood cells that enter the anterior chamber from sources in the posterior part of the eye through the pupil. We aim to identify the concentration of the particles at different locations inside the eye released from different sources of bleeding.

Leukocytes (WBC). WBC or leukocytes are rounded slightly flattened, nucleated cells, mainly protoplasmic in composition, and possessing contractile power. The average size is $\sim 10\ \mu$m [24], and they are present in blood in much smaller numbers than the red blood cells. The density of leukocytes is close to the fresh red blood cells [5]. They have the property of stickiness; thus, they can either clump together or stick with the ocular tissues. The average number of leukocytes in a normal adult varies between $5000/\text{mm}^3$ and $9000/\text{mm}^3$. When accumulation of leukocytes is mild, it is known as *keratic precipitates*. Keratic precipiates does not affect vision generally, but when they accumulate in sufficient amount at the bottom of the anterior chamber, a layered white structure is formed (Fig. 1(*d*)), which is known as hypopyon [29]. Hypopyon is an indication of severe intraocular inflammation inside the anterior chamber and may lead to damage of ocular tissues and loss of sight [29].

Mathematical Model

Geometrical Model of Rabbit's Eye. In this paper, attention is focused on a rabbit's eye (Fig. 2(*a*)), whose shape and geometry are slightly different from those of the human eye. The depth of the anterior chamber of the rabbit eye is in the range of 5–6 mm (as opposed to the human eye where the depth of the anterior chamber is in the 2–3 mm range), and diameter in the plane of the iris root is 12 mm. The iris, which is the front extension of the ciliary body, has a slightly elliptical shape with a vertical axis 11–12 mm long. The pupil changes its diameter depending on the amount of the light falling on the eyeball. It has been experimentally found that iris tissue is incompressible and linearly elastic under small deformations [3]. The biconvex crystalline lens located at the back of the anterior chamber is enclosed in a capsule suspended by the ciliary body with zonular fibers. AH secreted in the posterior chamber by the ciliary body enters the anterior chamber through the small gap between the iris and lens which is estimated to be few microns ($\approx 10\ \mu$m) [17].

In this paper, the anterior chamber of the rabbit's eye is modeled as a hemispherical geometry with a diameter of 6 mm (Fig. 2(*b*)). The iris is modeled as a rigid surface at the bottom of the hemispherical anterior chamber with a circular aperture at the center (the pupil) from which the flow enters the anterior chamber of the eye. It is assumed that neglecting the curvature of the iris surface and modeling it as a smooth annular surface will incorporate only minor error in the simulation results. Since the velocity profile and the flow pattern in the anterior chamber is buoyancy driven, it is unlikely that the inlet profile will have significant effect. This has been demonstrated in an earlier paper by the authors [6], and discussed further later. Therefore, for simplicity we have assumed a flat inlet velocity profile of AH through the pupil (of radius 2.5 mm).

The cornea is avascular and a transparent tissue with thermal properties close to that of water. It is modeled as a rigid hemispherical shell with a constant temperature (T_C). The temperature drop between the iris and the cornea (generally considered to be in the 2–4°C for the open eye) provides the buoyant force mechanism to drive the AH. The AH is assumed to be linear viscous liquid with properties close to those of water. The properties used in the present simulations are listed in Table 1.

The TM is a complex annular porous matrix located in the inner limbus close to the iris root (Fig. 2(*c*)). The outermost TM location is adjacent to the Schlemm's canal; the inner boundary of the TM directly borders the anterior chamber. In our simulations, TM is modeled as an annular porous zone (Fig. 2(*d*)), which is surrounding the anterior chamber close to the iris (Fig. 2(*b*)). It is assumed to have a thickness of 1 mm and an annular width of 1.2 mm. The part of TM adjacent to the anterior chamber is the uveal meshwork followed by the corneoscleral meshwork. This part of the meshwork has negligible resistance to the outflow due to its bigger pore size. We treat this part of TM as a porous jump interior surface at the entry of the annular porous zone with 0.2 mm thickness and a resistance coefficient corresponding to 50 μm pore size. The porous jump interior surface is treated as a thin porous medium of finite thickness over which the pressure change is defined as a combination of Darcy's law and an additional inertial loss term. The pressure gradient across the porous jump surface is given by Eq. (4). The coefficients of this equation are based on a porous bed of 0.5 void fraction and 50 μm mean pore size. The remaining part of TM (annular width of 1 mm) primarily represents the JCM and is treated as a porous zone (packed bed) with a specified average pore size of 0.6 μm and a void fraction of 0.5. Additional discussion on the selection of the TM characteristics is provided later.

Governing Equations. The steady three-dimensional incompressible Navier-Stokes equations are solved with the inclusion of buoyancy terms for natural convection [31,32] and Darcy pressure drop terms in the porous zone. The density appearing in the buoyancy term is assumed to satisfy the Bousinesq approximation. The resulting nondimensional forms of the momentum and energy equations are

$$\text{Momentum equation: } U_j\frac{\partial U_i}{\partial X_j} = \frac{1}{\text{Re}_D}\left(\frac{\partial^2 U_i}{\partial X_j \partial X_j}\right) + \delta_{im}\left(\frac{\text{Gr}_D}{\text{Re}_D^2}\right)\theta - \frac{\partial P}{\partial X_i} + S \quad (1)$$

where m represents the index of the coordinate direction along which gravity is acting and S is the sink term representing the additional pressure drop in the porous regions and is added in the momentum equation only for the TM porous zone. The second term on the right-hand side of Eq. (1) (buoyancy term) is included in the momentum equation only for the coordinate direction in which body forces are acting (gravity forces)

$$\text{Energy equation: } U_j\frac{\partial \theta}{\partial X_j} = \frac{1}{\text{Pr}_D}\frac{1}{\text{Re}_D}\left(\frac{\partial^2 \theta}{\partial X_j \partial X_j}\right) \quad (2)$$

$$\text{Continuity equation: } \frac{\partial U_j}{\partial X_j} = 0 \quad (3)$$

The following nondimensional variables are used in Eqs. (1)–(3):

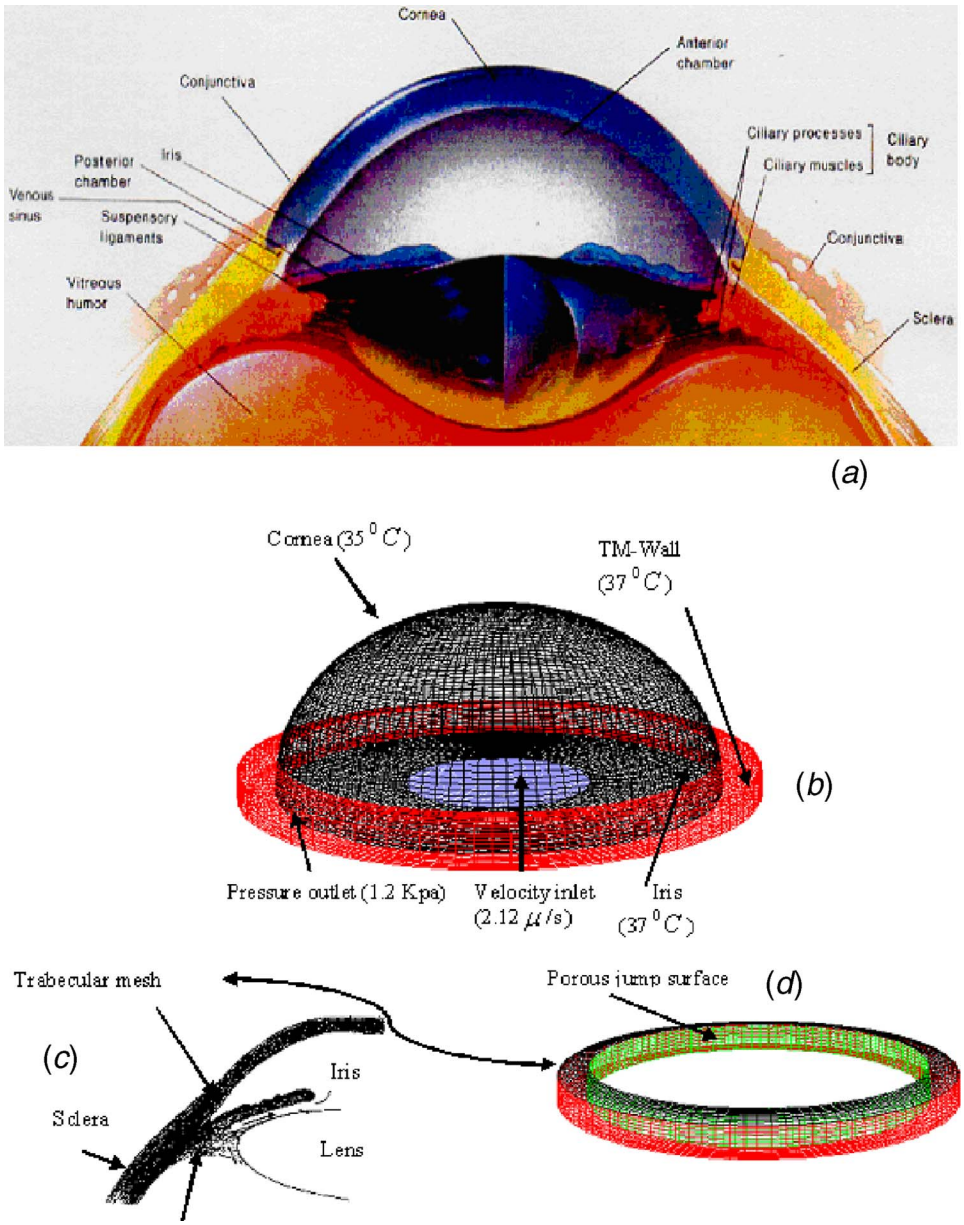

Fig. 2 (*a*) Schematic of a Rabbit's eye (from [29]), (*b*) geometrical model used for the simulation, (*c*) details of the anterior chamber (from [30]), (*d*) model of TM

$$X = \frac{x}{D}, \quad Y = \frac{y}{D}, \quad Z = \frac{z}{D}; \quad U = \frac{u}{U_{\text{in}}}, \quad V = \frac{v}{U_{\text{in}}}, \quad W = \frac{w}{U_{\text{in}}};$$

$$\theta = \frac{T - T_C}{T_{\text{in}} - T_C}; \quad P = \frac{p}{\rho U_{\text{in}}^2}$$

where T_{in} is the temperature of AH at inlet and T_C is the corneal temperature. The characteristic speed U_{in} (400 μ/s) is the average velocity in the anterior chamber and the characteristic length D (12 mm) is the diameter of the iris surface in the model.

Table 1 Properties of AH used in simulations

Properties	Value
Dynamic visocity (μ, Kg/ms)	0.001
Specific heat (C_p, J/Kg K)	4182
Density (ρ, Kg/m^3)	1000.0
Thermal conductivity (K, W/m K)	0.6
Volume expansion coefficient (β, 1/K)	0.0003

The important nongeometrical parameters that appear in the governing equations and their values of interest in the present study are

$$\text{Re}_D{:}4.8 \left(\text{Reynolds number, } \text{Re} = \frac{\rho U D}{\mu} \right)$$

$$\text{Pr}{:}7.0 \left(\text{Prandtl number, } \text{Pr} = \frac{C_p \mu}{K} \right)$$

$$\text{Gr}_D{:}1.017 \times 10^4 (\Delta T = 2\ ^\circ\text{C})$$

$$\left(\text{Grashof number, } \text{Gr}_D = \frac{D^3 \rho^2 g \beta \Delta T}{\mu^2} \right)$$

To model the porous region representing the TM, the dimensional momentum sink term ($\Delta P/L$) is the sum of a viscous loss term and an inertial loss term. Thus,

$$\frac{\Delta P}{L} = \frac{\mu}{\alpha} u_i + C_2 \frac{\rho}{2} |u_i| u_i \tag{4}$$

which is added in momentum equation (1) in nondimensional form as $S=(D^2 U_i/\alpha \mathrm{Re}_D)+(C_2/2)D|U_i|U_i$. This term is not included in the momentum equation for the nonporous fluid zone. The momentum sink contributes to the pressure gradient in the porous cell, creating a pressure drop that is proportional to the fluid velocity (first term) and velocity squared (second term) in the cell. The porous media model incorporates an empirically determined flow resistance in the porous region. In laminar flows through porous media, the pressure drop is typically proportional to velocity. Thus, the viscous term (first term) in Eq. (4) is more important with respect to the inertial resistive term (second term). Here, α is the permeability and C_2 is the inertial resistance factor. To get appropriate values of the constants α and C_2, a semiempirical correlation, derived from the Ergun equation [33], is used. These correlations for the permeability α and inertial resistance factor C_2 are applicable over a wide range of Reynolds number and for various packing levels and are given as

$$\alpha = \frac{D_p^2 \varepsilon^3}{150(1-\varepsilon)^2}; \quad C_2 = \frac{3.5(1-\varepsilon)}{D_p \varepsilon^3}$$

where D_p is the mean particle diameter of the packed bed and ε is the void fraction. The void fraction ε is defined as the volume of the voids divided by the volume of the packed bed. The particle diameter D_p of the packed bed for the porous medium in TM is evaluated by the relation $[\varepsilon/(1-\varepsilon)D_p=d]$, where d is the pore size. It is assumed that each particle is accompanied by one pore space. The pore size used in present study is 0.6 μm, and the value of ε is taken as 0.5. Justification for this is given later.

Particle simulation. For the present simulations, pigment particles are considered as spherical particles of diameter of 1 μm, RBC as particles of diameter 5 μm and WBC as particles of diameter 10 μm. These particles are small in size (low Stokes number), and therefore, it is assumed that the flow field is unaffected by the particle motion. Trajectories of these discrete phase particles is predicted by integrating the force balance equations of the particle in a Lagrangian reference frame. This force balance equates the particle inertia with the other forces acting on the particle. This force balance is represented in the x_i direction as

$$\frac{du_{i,p}}{dt} = F_D(u_i - u_{i,p}) + \frac{g_i(\rho_p - \rho)}{\rho_p} \tag{5}$$

where

$$F_D = \frac{18\mu}{\rho_p d_p^2} \frac{C_D \mathrm{Re}}{24}$$

Here, F_D is the drag force, Re is relative Reynolds number, and C_D is drag coefficient of the particle, which are expressed as

$$\mathrm{Re}_p = \frac{\rho d_p |u_p - u|}{\mu}; \quad C_D = \frac{24}{\mathrm{Re}}(1 + b_1 \mathrm{Re}^{b_2}) + \frac{b_3 \mathrm{Re}}{b_4 + \mathrm{Re}}$$

For spherical particles, the constants are given as $b_1=0.196$, $b_2=1.921$, $b_3=0.437$, $b_4=7185.35$ [34]. For a typical case of particle simulation, when fluid velocity is 1 mm/s and difference of particle velocity from fluid velocity is 0.1 mm/s, the relative Reynolds number Re_P is calculated as 0.1 and the Stokes number $(\rho_d d_p^2 u/18\mu a)$ is 1.88×10^{-4}. All the simulations are carried out with the assumption that particles have spherical shape and smooth surface. It is assumed that all body forces acting on the particle are constant, and Eq. (5) is linearized such that the trajectory equation can be rewritten in a simplified form as

$$\frac{du_{i,p}}{dt} = \frac{1}{T_p}(u_i - u_{i,p}) \tag{6}$$

The particle trajectory is itself computed by

$$\frac{dx_i}{dt} = u_{i,p} \tag{7}$$

Equations (6) and (7) are solved simultaneously to determine the velocity and position of the particle at any given time. The time step for the particle simulations is determined by $\Delta t = L/(u_p+u_c)$, where L is the distance traveled by the particle before its equations of motion are solved again and trajectory is updated, u_p is the magnitude of the particle velocity, and u_c is the magnitude of the velocity of the continuous phase. The length scale L should be representative of the mesh sizes, and in the present study, a length scale of 0.1 mm is used for the present particle simulations. The maximum number of time steps used in our simulation is 100,000, after which the trajectory calculation for the current particle injection is stopped. The particles remaining in the anterior chamber are those that are unable to come out from the anterior chamber. They are either trapped in the recirculation region or have very low velocities (long residence times) and are considered to be deposited on an ocular tissue surface. For the interaction of the particle with ocular tissues (corneal, iris, and TM surfaces), constant value of coefficient of restitution (0.5) is set for both normal and tangential directions. This means that if a particle hits any ocular surface, then after the impact its velocity is reduced in magnitude to half of its previous value in both the normal and tangential direction of the wall surface. The coefficient of restitution represents the "stickiness" of the particle and plays a role in determining the fate of the particles after they strike the ocular surfaces of the anterior chamber. The value of coefficient of restitution assumed for the present particle simulations implies that if the particle velocity is small in magnitude at any particular location close to the ocular surface and flow is not able to sweep away these particles, then after few impacts from the ocular surface the magnitude of velocity get reduced to negligible value. The movement of the particle at that particular location will be small (large residence times), and the particles can then be considered to have deposited at that particular location. The accumulation of these particles is responsible for the formation of specific structures observed in the eye such as Krukenberg's spindle, hyphema, or hypopyon.

The pigmentary particles are of the order of 1 μm, and are of the same order as the smallest pores in the TM. Therefore, the small pigment particles are allowed to enter into the pores of TM without any obstruction. However for the larger particles, since the actual morphological geometry and the particle-trapping mechanisms are not clearly understood, it is very difficult to exactly model such complicated tissue-particle interaction using present computational tools. Our goal is not to simulate these complex interactions, but we recognize that smaller particles travel through the TM unimpeded while the larger particles experience appreciable flow resistance. Therefore, for the bigger particles (RBC and WBC), the porous jump surface is treated as a reflecting surface with constant coefficient of restitution (0.5) to slow down and prevent the bigger particles from entering the smaller pores of the JCM in the TM. The pressure outlet boundary is a nonreflecting boundary and allows the particles, if they arrive, to exit this boundary smoothly. Therefore, the particles which reach the TM outlet (pressure outlet boundary) escape from the solution domain, and are considered to drain out through the aqueous veins.

Boundary Conditions. The iris and cornea are modeled as stationary rigid boundaries, and no-slip boundary conditions are imposed along these surfaces. The normal secretion rate from ciliary body is 2.5 μL/min, and to satisfy this inlet flow rate through the pupil (circular aperture of radius 2.5 mm), a flat inlet flow profile

of 2.12 μm/s magnitude is used for all simulations. Since most of the flow drains out to aqueous veins passing radially through the TM and the collector channels, the upper and lower surfaces of the annular TM are assumed to be impermeable walls (no-slip boundary condition). The pressure in the aqueous veins under normal condition is 9 mm of Hg [6], so the outlet boundary (exit of TM) is treated as pressure outlet boundary condition with a specified pressure of 9 mm of Hg (1.2 kPa). The inclusion of the TM in the present simulation, and the incorporation of a realistic pressure outlet boundary condition, is a distinct improvement over previously reported efforts [3–6,15–17].

For the temperature, the iris and the incoming flow through the pupil are specified to be at the core body temperature (37°C). The temperature of the cornea is set at constant value of 308 K. The small temperature difference between the corneal and iris surface drives the flow inside the anterior chamber since buoyancy is the dominant flow mechanism inside the eye.

Numerical Procedure

The numerical procedure is based on a control-volume approach where the computational domain is divided into a number of cells or elements, and the governing equations are discretized into algebraic equations in each element. The control-volume approach leads to discretization equations, which express the integral conservation of mass, momentum, and energy over each control volume. The discrete values of the variables are stored at the cell centers, but the convection terms in the discretized equation must be interpolated at the cell faces from the cell-center values. A second-order upwind scheme is used for deriving the face values of different variables in the momentum and energy equations. For the pressure Poisson equation, a second-order accurate discretization scheme is used. For preserving second-order accuracy, a multidimensional linear construction approach is used to compute the quantities at the cell interfaces. In this approach, Taylor-series expansion of the cell-centered solution about the cell centroid is used, and the face value ϕ is computed using $\phi_f = \phi + \nabla\phi.\Delta\vec{S}$, where ϕ is the cell-centered value in the upstream cell and $\Delta\vec{S}$ is the displacement vector from the upstream cell to the face centroid.

A structured multiblock solver is used for the numerical solution. The system of algebraic equations is solved using Gauss-Siedel scheme. Although the Gauss-Siedel scheme rapidly removes the high-frequency errors in the solution, low-frequency errors are reduced at a rate inversely related to the grid size. For computations with a large number of nodes, the solver stalls and the residual reduction become prohibitively slow. A V-cycle multigrid scheme is used to accelerate the convergence by applying corrections on the coarser grid levels. The coupling between velocity and pressure is handled using the SIMPLEC algorithm [35], which uses the conservation of mass equation to derive a pressure corrector equation, and uses a pressure and velocity correction step to yield continuity satisfying velocity fields at each iteration.

In the porous medium region, the pressure drop appears as a momentum source term, which yields a loss of diagonal dominance and poor convergence rates. To avoid exacerbating convergence issues, it is critical to have high-quality orthogonal grids with moderate aspect ratios. The commercial package GRIDPRO was used in the grid-generation process and only hexahedral cells of aspect ratio <3 in the computational domain is used. The entire geometry is divided into 29 blocks with four blocks representing the porous zone, five blocks located in the core of the hemispherical anterior chamber, and the remaining 20 blocks defining the periphery (Fig. 3(*a*)). For the cases reported in this paper, 300,000 hexahedral cells are used. To demonstrate grid independence, simulations are run with 600,000 and 1,000,000 cells. Less than 2% variation in the magnitude of the maximum velocity is observed between the 300,000 cell calculation and the 1,000,000 cell calculation (Fig. 3(*b*)) and justifies the use of 300,000 cells for the simulations.

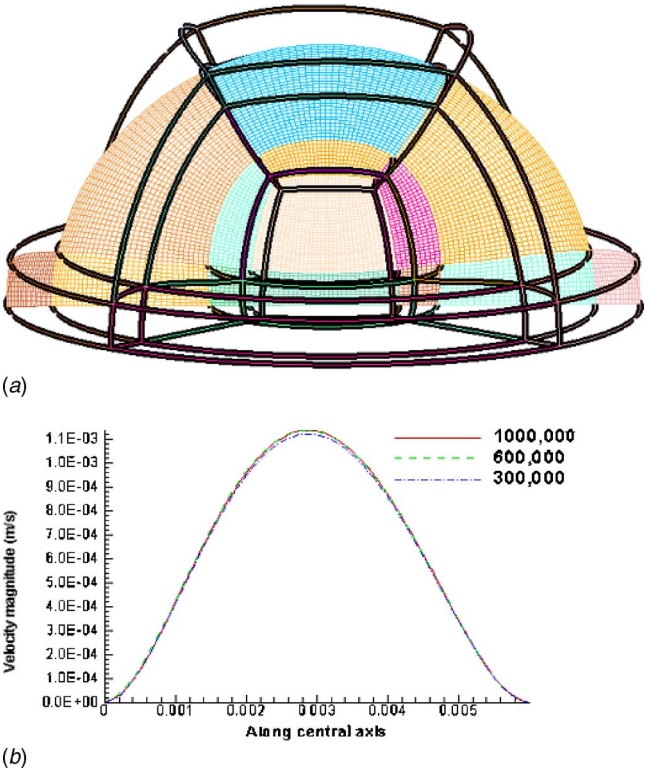

Fig. 3 (*a*) Blocks of the topology and mesh in the model in vertical midplane and (*b*) velocity magnitude along the central axis of the anterior chamber for 300,000, 600,000, and 1000,000 hexahedral cells

Results and Discussions

Flow Results. The flow calculations are obtained for two different orientations of the eye. As noted earlier, particle simulations are performed in an uncoupled manner, where it is assumed that flow profile is not affected by the particle motion. Gravity plays a major role in determining the flow pattern of AH inside the anterior chamber. In the horizontal upward-facing position (Fig. 4(*a*)) the gravity direction is perpendicular to the iris surface, and the flow field is axis-symmetric. In the vertical orientation (Fig. 4(*b*)), gravity destroys the symmetry in the vertical (*Y*-*Z*) plane. For

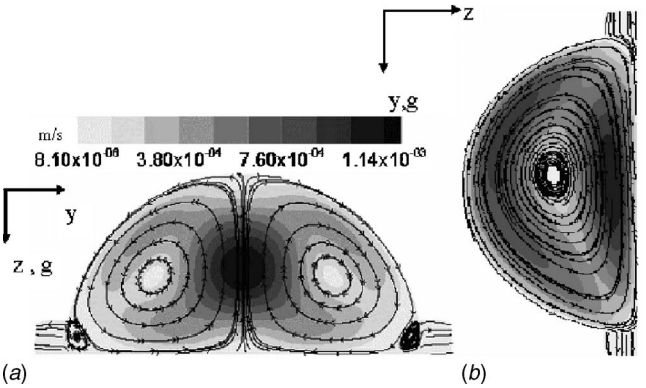

Fig. 4 Streamlines and contours of velocity magnitude: (*a*) horizontal orientation, vertical midplane; and (*b*) vertical orientation, vertical midplane. $\Delta T = 2°C$, pore diameter = 0.6 μ

Table 2 IOP as a function of pore size and pore diameter in the JCM

Porosity ε	Pore size d	Pore diameter D_p	IOP (KPa)	IOP (mm Hg)
0.5	0.6	0.6	1930.000	14.476
0.25	0.9	2.7	1894.000	14.206
0.2	1.0	4.0	1875.000	14.063

these two orientations, the flow profiles and recirculation zones are completely different. For the horizontal position, the warmer fluid entering the pupil rises upward and moves down the corneal surface leading to two large symmetric recirculation zones. The highest velocities (1.14 mm/s) occur midway along the vertical axis of symmetry. Just next to the TM there is a smaller recirculation zone, which shows the effect of the resistance of TM on the outflow. All features of the flow field are identically the same about the vertical axis of symmetry, including the exit flow rates through the left and right TM. For the vertical orientation of the eye, the warmer fluid rises upward along the iris surface and then turns downward as it encounters the higher resistance in the upper TM regions. The flow then descends along the corneal surface toward the lower TM and exits through the small pores of the TM. Furthermore, no secondary eddy is observed in the vicinity of the TM as in the horizontal configuration. The stagnation zones and regions of large curvature are of special interest because particles present in the AH can get trapped in these regions and can lead to the development of specific structures. For both the orientations, the magnitude of the flow velocity decreases as AH flows out from anterior chamber to aqueous veins through TM.

Selection of Pore Size and Porosity. Simulations are performed with different values of porosity reported in the experimental studies. The simulations with porosity of 0.5 and pore size of 0.6 μm is representative of the studies reported by Lindenmayer et al. [14] and are used in the present study. The IOP of the eye for this case is found to be 14.47 mm of Hg. Lutzen-Drecoll [36] has reported that the optical clear space of JCM as 17 ± 7.7 %, while Ethier et al. [37] has reported it as 23 ± 4.6 %. Thus, there is some scatter in the porosity values reported. To analyze the effect of this scatter, additional simulations are performed with 0.25 and 0.2 porosity values to cover the spectrum of porosity values reported from 0.5 [14] to 0.17 [36]. It is observed (Table 2) that for porosity of 0.25 and pore size of 0.9 μm, the IOP of eye is 14.206 mm of Hg, which is close to the IOP with the porosity of 0.5 and pore size of 0.6 μm. For porosity of 0.2 and pore size of 1.0 μm the IOP is 14.063 mm of Hg, which is again close to the IOP of eye observed in simulations with porosity of 0.5 and pore size=0.6 μm or porosity of 0.25 and pore size=0.9 μm. The pore size of TM for which achieved IOP of eye is close to IOP of normal eyes (14–15 mm of Hg) lies in the range of 0.1–1 μm, which is representative of the pore size of JCM reported by experimental studies [12]. These results indicate that realistic IOP of eye and realistic pressure drop across the ocular drainage system can be obtained by several combinations of the pore size and porosity values that lie in the range of values reported in experimental studies. For the simulations in the present study, the porosity of TM is considered as 0.5 and pore size as 0.6 μm [6] for all particle simulations.

Effect of Inlet Profile. For analyzing the effect of inlet velocity profile, simulations are performed for the flat velocity profile and parabolic velocity profile at the inlet aperture of the anterior chamber. No significant difference is observed in the velocity magnitude in the anterior chamber for two different inlet profiles. This again shows that flow field inside the anterior chamber is not much affected by the inlet velocity profile since the mass flow rate is not altered and buoyancy is the dominant flow driving mechanism. This justifies the use of flat velocity profile inside the anterior chamber.

Particle Trajectories. Figure 5 shows the trajectories of 1 μm dia particles (pigmentary cells) released from the various circumferential positions at different radii located on the pupil surface or the iris surface. The gray scale represents the particle residence time. The injection through the pupil implies that the origin of the particles is in the posterior chamber and that the particles are entrained into the posterior AH flow and enter the anterior chamber through the pupil. For the vertical orientation of the eye, particles released from the pupil surface rise against gravity moving along the iris surface. When higher resistance is encountered near the upper part of TM, the flow turns and descends along the corneal surface and exit through the lower TM. Most of the particles come out from the lower part of the TM, but several particles (with sufficient momentum) are seen to turn the lower corner and rise up the middle portion of the anterior chamber and exits from the TM along the mid-horizontal plane (Fig 5(*a*)). The average time spent by most of the particles is around 2200 s (37 min) (Table 3). Particles released from the central portion of the pupil surface spend more time in the anterior chamber compared to the other particles. As the radius of the circles in the pupil opening from where particles are released is increased, the time spent by the particles in the anterior chamber decreases (Table 3). Particles released from the iris surface have trajectories similar to the particles released from the pupil surface except that a number of particles exit from the top of the TM (Fig. 5(*b*)). This difference between particles released through the pupil versus those released from the anterior iris surface is observed because the particles released from the pupil surface circulate in the vicinity of the vertical midplane passing through the central axis, while particles released from the iris surface circulate in the off-center planes parallel to the vertical midplane. Because of strong flow in the vertical midplane, particles released from the pupil surface have sufficient inertia as they reach the upper part of the TM and are therefore able to turn the corner and do not come out from the upper TM. The iris-released particles come out through the pores of upper TM since, in the other vertical planes, the flow has lower strength, and the particles have lower inertia as they reach the upper TM. As the distance of the point of release of the particles from the pupil center is increased, their residence time inside the anterior chamber decreases due to their greater propensity to leave through the upper TM.

The particles released from the root of the iris show a completely different behavior. They exhibit a bimodal behavior in terms of residence time with some particles spending a minimum amount of residence time (867 s) and some particles spending considerably greater time (6064 s) inside the anterior chamber (Table 4). This is consistent with the flow field observed next to TM, where the flow has sharp curvature and the magnitude of flow velocity is very low. Therefore, particles in the middle of the recirculation region keep recirculating near the TM and have long residence time in the anterior chamber. However, particles along the outer edge of the corner eddy are able to penetrate the TM and therefore escape from the anterior chamber in a minimum amount of time (Table 4).

In general, the pigment particles have maximum residence time along the lower portion of the cornea or inside the pores of TM (Figs. 5(*a*) and 5(*b*)). This reflects the possibility that these particles deposit in the endothelium layer along the lower corneal surface, which, in turn, could lead to the formation of spindlelike structures along the lower part of the cornea (KS) (Fig. 1(*b*)). Alternatively, they could clog the pores of TM and can lead to elevation in IOP of the eye.

For horizontal orientation of the eye, the particles released from the iris surface rise against gravity along the axial direction toward the central portion of the cornea and after encountering the

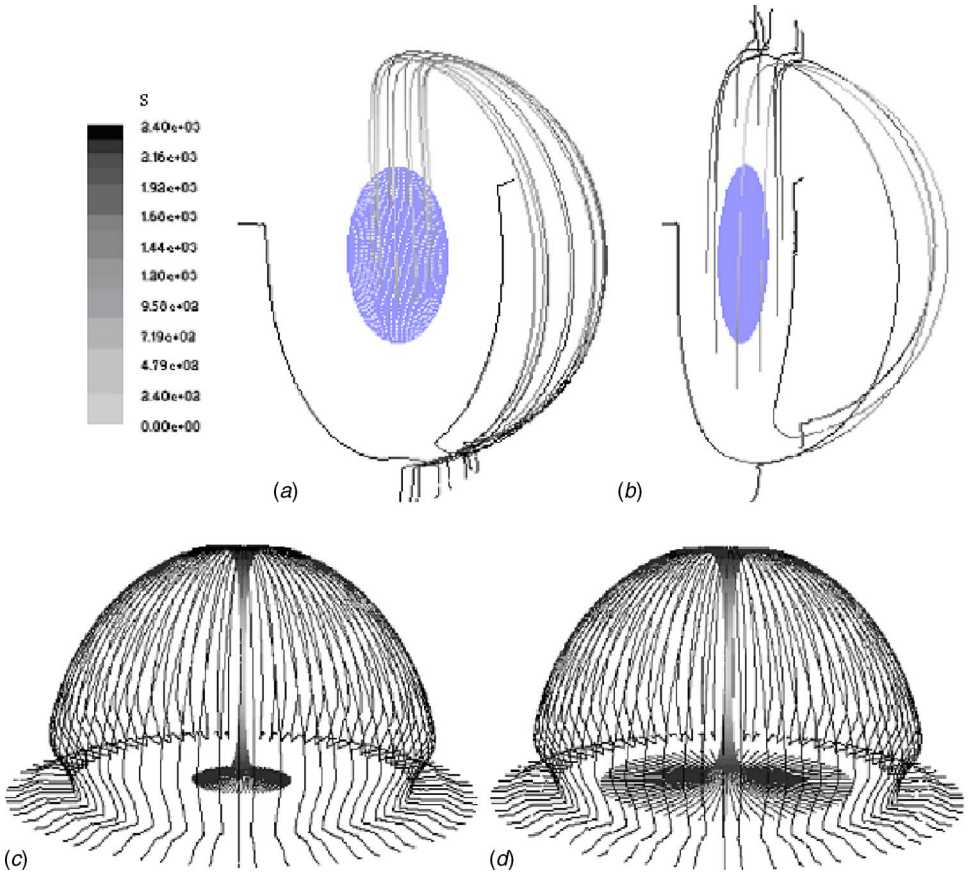

Fig. 5 Particle trajectories and residence times for pigmentary granules: (*a*) particles released from the pupil surface located on the circumference of radius 1.5 mm, vertical orientation; (*b*) particles released from the iris surface located on the circumference of radius 3.8 mm, vertical orientation; (*c*) particles released from the pupil surface located on the circumference of radius 1.5 mm, horizontal orientation; and (*d*) particles released from the iris surface located on the circumference of radius 3.8 mm, horizontal orientation

resistance from the corneal surface they descend along the cornea. Because of the small vortex next to the TM, these particles do not descend all the way up to the iris root, but follow the vortex streamlines and strike the iris surface in a circular band of radius 5 mm from the pupil center (Fig. 5(*c*)). The average residence time of these particles is 1700 s (28 mins) as indicated in Table 5. The trajectories of these particles show high residence time near the central portion of the cornea and inside the pores of TM, which indicates the potential of these particles adhering to the central corneal endothelium or TM walls. When the particles are released from the iris surface, they follow the trajectories almost similar to the particles released from the pupil surface except that they come closer to the portion of the cornea next to the central region before descending along the corneal surface (Fig. 5(*d*)). There is a stagnation region on the iris surface next to the small vortex at the bottom of the anterior chamber, which is located approximately at a distance of 5 mm from the iris center. The particles released from this location have long residence times (1803 s) inside the anterior chamber. Particles released outside the region of 5 mm radius is affected by the small corner vortex next to TM and show different behavior from the particles released within the radius of 5 mm. When the particles are released from the region inside the radius of 5 mm, the minimum residence time (1690 s) corresponds to the particles released from the iris tip, which increases with the radius of point of release as shown in Table 6. Particles released from the iris root do not circulate inside the anterior chamber and come out through the TM in the shortest time (1458 s).

For analyzing the transport of erythrocytes and leukocytes, par-

Table 3 Time spent by particles inside anterior chamber when released from circumference of different radii on pupil surface (vertical orientation, particle diameter=1 μ)

Radius r (mm)	Minimum (s)	Maximum (s)	Average (s)
0.7	2083	2399	2197
1.0	2068	2446	2188
1.5	2079	2545	2197
2.0	1994	2396	2185
2.4	1895	2424	2151

Table 4 Time spent by particles inside anterior chamber when released from circumference of different radii on iris surface (vertical orientation, particle diameter=1 μ)

Radius r (mm)	Minimum (s)	Maximum (s)	Average (s)
2.6	1976	2347	2131
3.2	1873	2296	2109
3.8	1817	2334	2095
4.4	1769	2348	2045
5.0	1800	2440	2054
5.8	867	6064	2423

Table 5 Time spent by particles inside anterior chamber when released from circumference of different radii on pupil surface (horizontal orientation, particle diameter=1 μ)

Radius r (mm)	Average (s)
0.7	1737
1.0	1710
1.5	1694
2.0	1692
2.4	1688

Table 6 Time spent by particles inside anterior chamber when released from circumference of different radii on iris surface (horizontal orientation, particle diameter=1 μ)

Radius r (mm)	Average (s)
2.6	1690
3.2	1700
3.8	1711
4.4	1724
5.0	1803
5.8	1458

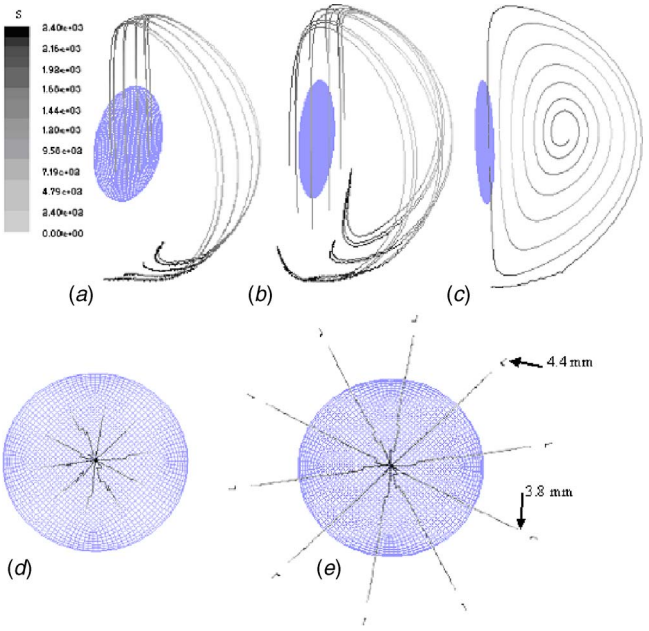

Fig. 6 Particle trajectories and residence time for erythrocytes: (*a*) particles released from the pupil surface located on the circumference of radius 1.5 mm, vertical orientation; (*b*) particles released from the iris surface located on the circumference of radius 3.8 mm, vertical orientation, (*c*) particle released from the center of the anterior chamber, vertical orientation; (*d*) particles released from the pupil surface located on the circumference of radius 1.5 mm, horizontal orientation; and (*e*) particles released from the iris surface located on the circumference of radius 3.8 mm (inner trajectory) and 4.4 mm (outer trajectory), horizontal orientation

ticles of diameter 7 μm and 10 μm are released from the iris and pupil surface and both of them follow almost similar trajectories inside the anterior chamber. For the vertical orientation of the eye, particles released from the pupil surface rise along the iris surface and then descend along the cornea due to the high resistance encountered from the upper part of TM. These particles are not swept away by the exiting flow when they reach the bottom of the anterior chamber and get deposited on the ocular tissues (Figs. 6(*a*) and 6(*b*)), which is evident from the high residence time of these particles at the bottom portion of the anterior chamber. The deposition of these particles is linked to the formation of layered hyphema or hypopyon at the bottom of the anterior chamber.

For the horizontal orientation of the eye, the particles released from the pupil surface move toward the center of the pupil. These heavier particles are not able to rise against the gravity and show tendency of getting accumulated in the central region, Fig. 6(*d*). Particles released from the iris surface within the radius of 3.8 mm move toward the center, but particles released from locations outside this region (at 4.4 mm as shown in Fig. 6(*e*)) move around their point of release, which indicates that these particles can be trapped on the iris surface (Fig 6(*e*)). Particles released from the center of the vertical midplane of anterior chamber continue circulating with increasing diameter in the vertical plane. As the particles come close to the ocular tissues at the bottom of the anterior chamber, they get deposited there (Fig. 6(*c*)). This observed behavior of the particle released from the center of the anterior chamber is in agreement with the results of Heys and Barocas [5].

Krukenberg's Spindle. The deposition of pigment particles on the corneal surface leads to the formation of vertical spindlelike structure known as Krukenberg's spindle. There are regions inside the anterior chamber where the flow takes sharp bend and stagnates due to the resistance of the ocular tissues (Fig. 4). These are the regions where the deposition of the particles is likely to occur (Figs. 5 and 6), due to large residence times and high particle concentrations, and once the particles aggregate on the ocular tissues, flow is unable to sweep away and relocate these particles. Particles continue accumulating in these regions and spindle shaped structures are formed on the ocular surface. Evidence of this is provided here by looking at particle concentration distributions.

There are two sources of pigment granules inside the anterior chamber: (i) particles shed from the pigmentary layer of the posterior iris surface [18,38] that enter into the anterior chamber through the pupil and (ii) pigment particles that may be present on the anterior iris surface and are released directly into the anterior chamber. For analyzing the behavior of particles entering the anterior chamber through the pupil (representing particles shed from the posterior surface), particles are released from the points evenly spaced on the circumference of the circles of different radii located on the circular inlet aperture. Kuchle et al. [20] has reported in their experimental results on eye with PDS that 2.5 μl of the AH contains ~100 pigment granules. Particles are released from the circular aperture at 409 different locations, and their mass flow rate is kept constant such that the concentration of the pigment granules entering the anterior chamber would be in agreement with the experimental results of Kuchle [21]. Pigment particles generated from the anterior surface of the iris are modeled by releasing 72 particles from the circumference of every circle of radii varying from 2.6 mm to 5.8 mm (r=2.6, 3.2, 3.8, 4.4, 5.5, 5.8 mm) resulting in 432 particles. All these particles are released at the same time instance.

For the vertical orientation of the eye, when the particles are released from the pupil surface, the concentration of the particles is high at the mid-to-lower portion of the corneal surface, Fig. 7(*a*). The concentration of the particles on the iris surface is almost negligible except in the lower half of the TM, where the particles are coming out from the anterior chamber (Fig. 7(*b*)). The high concentration of the particles on the mid-to-lower corneal surface is consequence of the sharp bend of flow at the junction of the corneal and iris surface near the lower TM zone. The flow has lower velocities as it approaches the lower part of TM, and therefore, the light pigment particles sediment on the lower corneal surface as reflected by the high concentration of particles in that region. Accumulation of a central band of pigment particles

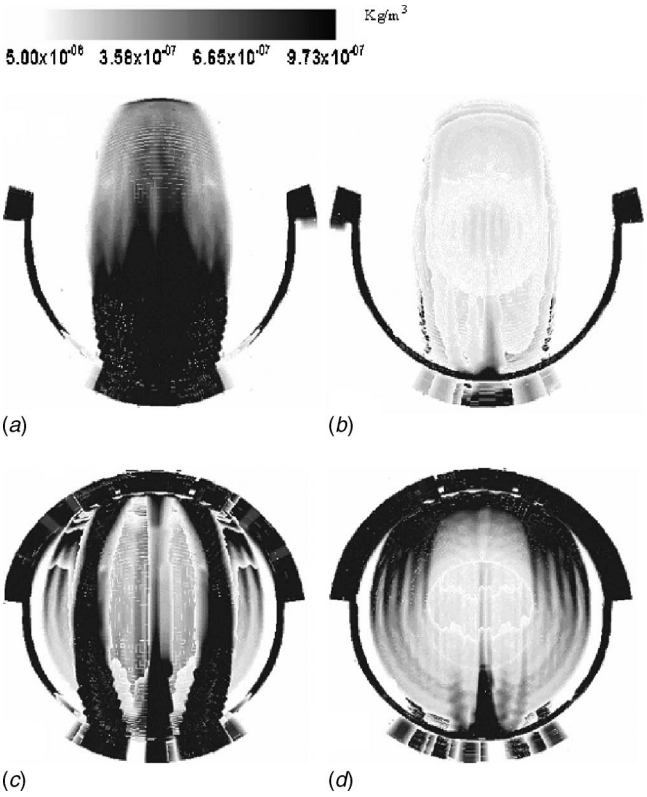

Fig. 7 Vertical orientation (pigment particles): (*a*) particles released from the pupil surface, view from corneal surface; (*b*) particles released from the pupil surface, view from iris surface; (*c*) particles released from the iris surface, view from corneal surface; and (*d*) particles released from the iris surface, view from iris surface

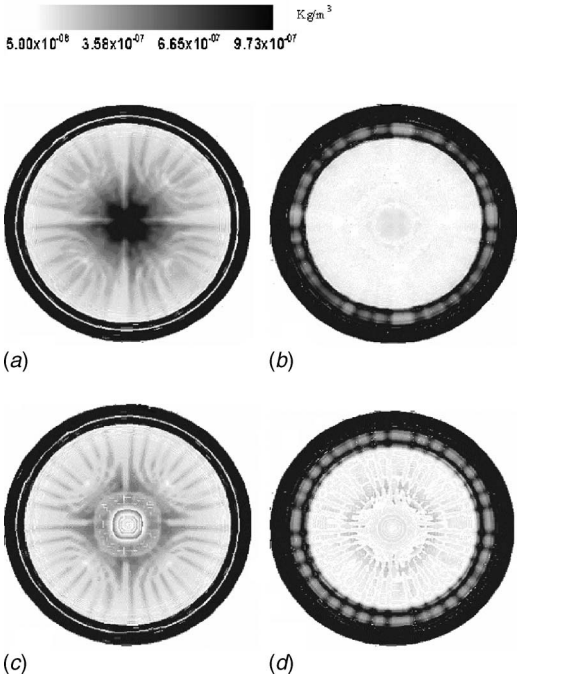

Fig. 8 Horizontal upward facing orientation (pigment particles): (*a*) particles released from the pupil surface, view from corneal surface; (*b*) particles released from the pupil surface, view from iris surface; (*c*) particles released from the iris surface, view from corneal surface; and (*d*) particles released from the iris surface, view from iris surface

on the lower portion of the corneal surface is consistent with the formation of KS structure, which is observed in certain clinical images of the eye (Fig. 1(*b*)). When the particles are released from the iris surface, three patches of higher concentration of pigment granules on the corneal surface is observed (Fig. 7(*c*)). The vertical patch of high concentration along the midpart of the cornea agrees with the formation of the KS structures or PDS and manifests itself as a vertical spindlelike structure on the midcorneal surface (Fig. 1(*a*)). Kampik et al. [39] have reported images of pigment granule deposition on the corneal endothelium as a vertical spindlelike structure from their results of microscopy on eyes with PDS. Their observation resembles the midpatch of high concentration in the present model.

High concentration of particles on the upper part of iris surface is also observed (Fig. 7(*d*)), originating from particles released from the iris surface. As these particles rise upward along the iris surface, their flow strength is reduced due to the resistance from the upper TM region. The particles, therefore, do not have sufficient inertia to negotiate the turning, and deposit in the vicinity of the low-velocity regions.

The concentration plots on the corneal surface are in agreement with the time residence plot by Heys and Barocas [5] on the corneal surface. They observed three vertical bands of high residence time on the corneal surface. The residence time is directly correlated with the concentration of pigment particles (reported here) on the corneal surface.

For the horizontal upward facing eye orientation, when the particles are released through the pupil (Fig. 8(*a*)), the particles entering with the AH rise upward against gravity and approach the central portion of the cornea. High concentration of particles is observed on the central corneal surface, where the flow stagnates due to impingement. This high concentration of pigment particles on the corneal surface is in agreement with the numerical simulation of KS formation resulting from flow through pupil aperture reported by Canning et al. [4]. On the iris surface, a circular band of high pigment concentration is observed close to the TM region (Fig. 8(*b*)). The high concentration of pigment granules in a circular band is consequence of a small corner vortex next to the TM region. The small corner recirculation zone forces the pigment particles falling down along the corneal surface to come close to the iris surface. The circular band of high pigmentation on the iris surface close to the TM region is supported by the experiments of Kampik et al. [39]. They found substantial amount of pigment particles in the anterior chamber angle for eyes with PDS.

The particles released from the iris surface exhibit deposition patterns (Figs. 8(*c*) and 8(*d*)) similar to those entering through the pupil. High concentrations are observed near the iris root, associated with the corner recirculation, and in the TM outflow pathway regions. Electron microscopy of TM by Kampik et al. [38] shows pigmented macrophages and pigmented endothelial cells within the TM, which supports the observation of high concentration of pigment granules in the entire TM region as observed in the present model predictions.

Hyphema. Hyphema is a common manifestation of accumulation of blood inside the anterior chamber of eye. For all simulations, performed with the present geometrical model concerned with blood accumulation, it is assumed that the main constituent of blood (i.e., erythrocytes) represents it completely. These particles are considered to be rigid with a diameter of 7 μm and density of 1500 Kg/m^3 [4]. For analyzing the erythrocytes generated from the sources located in the posterior chamber of eye and entering into the anterior chamber through the pupil with AH, particles are released from the points evenly spaced on the circumference of different radii circles located on the circular aperture of inlet. As with the simulation of pigment particles, 409 particles representing the erythrocytes are released from different

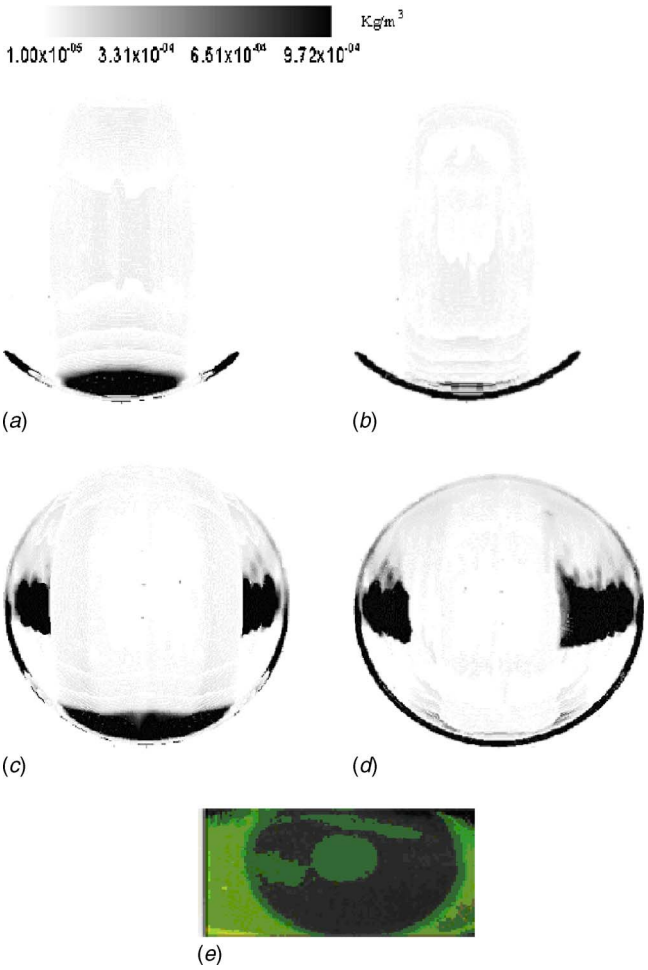

Fig. 9 Vertical orientation (RBC): (*a*) particles released from the pupil surface, view from corneal surface; (*b*) particles released from the pupil surface, view from iris surface; (*c*) particles released from the iris surface, view from corneal surface; (*d*) particles released from the iris surface, view from iris surface; and (*e*) corneal staining (showed using the same fluorescein dye) [41]

locations on the circular aperture with constant mass flow rate. To incorporate sources of bleeding from the disrupted blood arteries, iris vessels, ciliary body, or TM, where blood is directly released into the anterior chamber, the erythrocytes are modeled by releasing 72 particles from the circumference of every circle located on iris surface of radii varying from 2.6 mm to 5.8 mm (r=2.6, 3.2, 3.8, 4.4, 5.5, 5.8 mm).

The erythrocytes are much heavier than the pigment particles and show completely different behavior of deposition compared to the light pigment granules. For the vertical orientation of eye, particles released from the circular inlet aperture sediment at the bottom of the anterior chamber (Fig. 9(a)). There is almost negligible concentration of particles on the remaining part of the corneal or iris surface (Figs. 9(a) and 9(b)). The particles released from the pupil surface circulate in the region close to the central vertical plane and do not show any tendency to be deposited on the ocular tissues of the upper portion of anterior chamber. They gravitate downward inside the anterior chamber and give rise to the formation of layered hyphema. The shape of the layered structure formed by the sedimentation of particles is in close agreement with the shape of commonly observed grade-1 hyphema, where blood occupies less than one-third of the anterior chamber (Fig. 1(c)). The shape of hyphema predicted inside the anterior chamber resembles the images reported by Lai et al. [38] and Komaromy et al. [40]. Particles released simultaneously from different locations on the iris surface (Figs. 9(c) and 9(d)) show similar behavior with particles sedimenting to the bottom of the anterior chamber, but in addition, high concentrations are also observed along the midpart of the corneal and iris surface and closer to the junction of these two surfaces. Near the junction of the corneal and iris surface, the strength of the flow is low, and flow is not able to carry away the erythrocytes that have penetrated into this region. The pattern of deposition of these particles resembles the case of blood clotting on the iris surface or corneal blood staining in some cases of hyphema (Fig. 9(e)). Generally, corneal blood staining occurs primarily in patients who have total hyphema and associated prolonged elevation of IOP or if corneal endothelium has been damaged [27]; but in some rare cases, it may also occur in hyphema that is not grade 4, as shown in Fig. 9(e). In this case, sources are more distributed or blood is released at high rates [27]. In the present simulations, erythrocytes are released from the entire iris surface and represent the "distributed source" scenario, and the simulations are able to predict possible corneal blood staining or clotting on the iris surface, consistent with the clinical observations reported by Crouch and Crouch [28] and Wilson [27].

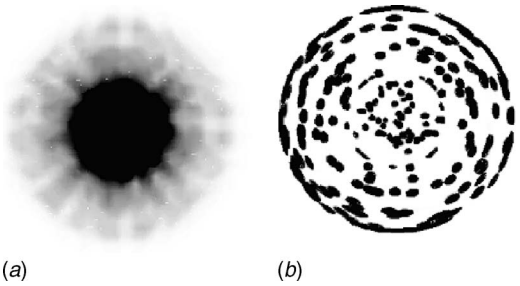

Fig. 10 Horizontal upward facing orientation (RBC): (*a*) particles released from the pupil surface, view from iris surface and (*b*) particles released from the iris surface, view from iris surface

For the horizontal orientation of the eye, particles released through the pupil has a tendency to move toward the center of the pupil and get accumulated there. These particles released from the different locations on the pupil surface are driven by the flow and move toward the center along the streamlines of the circulation vortex. When the flow rises against gravity along the axial direction, it is not strong enough to carry these heavy particles against the gravity and particles sediment at the lens close to the center, as shown in Fig. 10(a). Particles released from the iris surface get deposited on the iris surface in a distributed fashion and are also unable to rise against gravity (Fig. 10(b)).

Hypopyon. Accumulation of leukocytes inside the anterior chamber leads to the formation of layered structure commonly known as hypopyon. These structures are not commonly observed in normal eyes, but, when present, are an indication of inflammation in the anterior chamber. One of the objectives of the present model is to analyze the behavior of leukocytes, which are represented as rigid spherical particles of diameter 10 μm and density 1500 Kg/m^3 [4].

For the analysis of hypopyon formation, the simulations are performed again with two different sources of leukocytes (anterior chamber and posterior chamber). The rate of release of particles are kept constant at values similar to the simulations for erythrocytes. For the vertical orientation of the eye, the particles released through the pupil get sedimented at the bottom of the anterior chamber (as for the erythrocytes), but they do not deposit on other ocular tissues or exhibit staining characteristics (Figs. 11(a) and 11(b)). Particles released from the iris surface again show the same tendency to gravitate downward to the bottom of the eye (Fig. 11(c)). The shape of the hypopyon predicted by the present model resembles the images shown in Fig. 1(d) and reported by

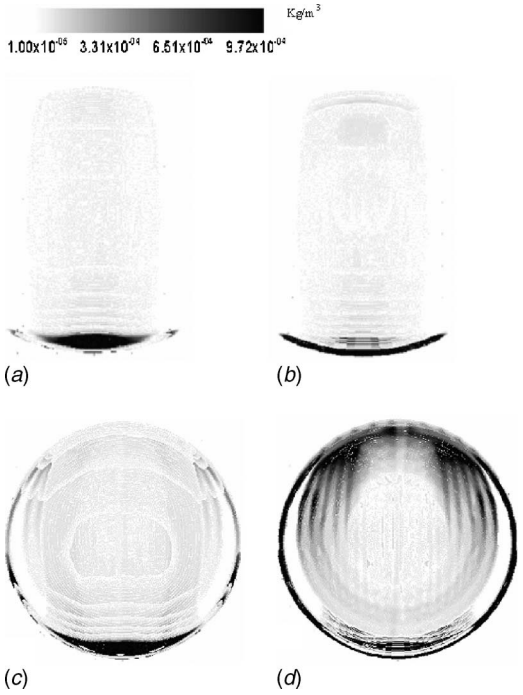

Fig. 11 Vertical orientation (WBC): (*a*) particles released from the pupil surface, view from corneal surface; (*b*) particles released from the pupil surface, view from iris surface; (*c*) particles released from the iris surface, view from corneal surface; and (*d*) particles released from the iris surface, view from iris surface

Alessandro et al. [29] and Olsen et al. [42].

High concentration of particles is also observed on the upper part of the iris surface, which is a consequence of low velocities due to the resistance from the upper part of the TM (Fig. 11(*d*)). There is no sign of deposition of particles along the mid corneal or iris surface as observed in the case of erythrocytes.

For the horizontal orientation of the eye, the simulations show that leukocytes behave like erythrocytes. When they are released from different locations on the pupil surface, they move toward the pupil center and get accumulated on the lens (as in Fig. 10(*a*)). When they are released from different locations on the iris surface, they get spatially distributed on the iris surface (as in Fig. 10(*b*)).

Concluding Remarks

Numerical simulations are performed on a three-dimensional model for the anterior chamber of the eye to investigate the transport and deposition of particles inside the eye. A geometrical porous-media model for the trabecular meshwork is included in the simulations, and the porosity and pore size values used are representative of those reported in the literature. The predicted IOP attained inside the anterior chamber matches the IOP reported for normal eyes. The particle simulations for different particle types are performed in a Lagrangian framework using the predicted AH flow field and pressure distribution. The primary contribution of the present paper is based on using a realistic representation of the TM and in analyzing particle deposition patterns for different particle types present in the AH and their origin.

Formation of three clinically observed structures, namely KS, hyphema, and hypopyon, are analyzed by using representative particles (pigmentary cells, erythrocytes, and leukocytes) of appropriate size and density. The interaction of the particles with ocular tissues is modeled by imposing suitable wall boundary and reflectivity conditions on the surfaces of the geometrical model. The numerical simulations provide concentration distributions that can be correlated with particle deposition patterns. For pigmentary cells, the simulations predict the accumulation of pigment granules along a vertical central band on the corneal surface with the highest concentration near the lower TM. This deposition pattern is consistent with the observed clinical images of KS. Simulation of heavier particles representing erythrocytes and leukocytes indicate that the majority of particles sediments to the bottom of the anterior chamber forming a layered structure similar to those observed in hyphema and hyopyon. Corneal blood staining or formation of clots on the iris surface, observed clinically for cases with distributed sources of blood cells, also are well predicted by the current model.

The qualitative agreement of the model predictions with the clinical observations enable the simulations to identify the origin and the mechanisms leading to the clinically observed conditions. Further refinement of the model (e.g., adhesion, deformation, coagulation, mechanical interaction with the pores in the TM, incorporation of the detailed TM structure including the Schlemm's canal, collector channels, etc.) would enable a more definitive understanding of the mechanisms leading to the various forms of eye diseases that are linked to deposition of different particle types. Various aspects of these refinements are currently in progress.

Acknowledgment

This work was supported by a grant from the Louisiana Health Excellence Research Program that established the Biological Computation and Visualization Center (BCVC) and is gratefully acknowledged.

References

[1] Mclaren, J. W., Trocme, S. D., Relf, S., and Brubaker, R. F., 1990, "Rate of Flow of Aqueous Humor Determined From Measurements of Aqueous Flare," Invest. Ophthalmol. Visual Sci., **31**(2), pp. 339–346.
[2] Tripathi, R. C., and Tripathi, B. J., 1984, "Anatomy of the Human Eye, Orbit, and Adnexa," *The Eye*, ed. H. Davson, Academic Press, New York, Vol. 1a, Vegetative Physiology and Biochemistry.
[3] Heys, J. J., Barocas, V. H., and Taravella, M. J., 2001, "Modeling Passive Mechanical Interaction Between Aqueous Humor and Iris," ASME J. Biomech. Eng., **123**, pp. 540–546.
[4] Heys, J. J., and Barocas, V. H., 2002, "Computaional Evaluation of the Role of Accommodation in Pigmentary Glaucoma," Invest. Ophthalmol. Visual Sci., **43**, pp. 700–708.
[5] Canning, C. R., Dewynne, J. N., Fitt, A. D., and Greaney, M. J., 2002, "Fluid Flow in the Anterior Chamber of a Human Eye," Mathematical Medicine and Biology, **19**(1), pp. 31–60.
[6] Kumar, S., Acharya, S., Beuerman, R., and Palkama, A., 2006, "Numerical Solution of Ocular Fluid Dynamics in a Rabbit Eye: Parametric Effects," Ann. Biomed. Eng., **34**(3), pp. 530–544.
[7] Okuno, T., 1991, "Thermal Effect of Infrared Radiation on the Eye: A Study Based on a Model," Ann. Occup. Hyg., **35**, pp. 1–12.
[8] Mori, A., Oguchi, Y., Okusawa, Y., Ono, M., Fujishima, H., and Tsubota, K., 1997, "Use of High-speed, High-resolution Thermography to Evaluate the Tear Film Layer," Am. J. Ophthalmol., **124**, pp. 729–735.
[9] Kocak, I., Orgul, S., and Flammer, J., 1999, "Variability in the Measurement of Corneal Temperature Using a Non-Contact Infrared Thermometer," Ophthalmologica, **213**(6), pp. 345–349.
[10] Johnson, M. C., Kamm., R. D., Grant, W. M., Epstein, D. L., and Gasterland, D., 1986, "The Flow of Aqueous Humor Through Micro-Porous Filters," Invest. Ophthalmol. Visual Sci., **27**, pp. 92–97.
[11] Ethier, C. R., Coloma, M. F., Kater, A. W., and Allingham, R. R., 1992, "Retroperfusion Studies of the Aqueous Outflow System," Invest. Ophthalmol. Visual Sci., **34**(2), pp. 385–394.
[12] Ethier, C. R., Kamm, R. D., Johnson, M., Pavoo, A. F., and Anderson, P. J., 1989, "Further Studies on the Flow of Aqueous Humor through Microporous Filters," Invest. Ophthalmol. Visual Sci., **30**, pp. 739–746.
[13] Kathawate, J. G., Master's thesis, http://etd.lsu.edu/docs/available/etd-11152006-214523
[14] Lindenmayer, J. M., Kahn, M. G., Hertzman, E., and Epstein, D. L., 1983, "Morphology and Function of the Aqueous Outflow System in Monkey Eyes Perfused With Sulfhydryl Agents," Invest. Ophthalmol. Visual Sci., **24**, pp. 710–717.
[15] Scott, J. A., 1988, "A Finite Element Model of Heat Transport in the Human Eye," Phys. Med. Biol., **33**, pp. 227–241.
[16] Scott, J. A., 1988, "The Computation of Temperature Rises in the Human Eye Induced by Infrared Radiation," Phys. Med. Biol., **33**, pp. 243–257.
[17] Heys, J. J., and Barocas, V. H., 2002, "A Boussinesq Model of Natural Convection in the Human Eye and the Formation of Krukenberg's Spindle," Ann.

Biomed. Eng., **30**, pp. 392–401.
[18] Epstein, D. L., Freddo, T. F., Anderson, P. J., Patterson, M. M., and Chu, S. B., 1986, "Experimental Obstruction to Aqueous Outflow by Pigment Particles in Living Monkeys," Invest. Ophthalmol. Visual Sci., **27**, pp. 387–395.
[19] Lehto, I., Ruusuvaara, P., and Setala, K., 1990, "Corneal Endothelium in Pigmentary Glaucoma and Pigment Dispersion Syndrome," Ophthalmologica, **68**, pp. 703–709.
[20] Rodrigues, M. M., Spaeth, G. L., Weinreb, D., and Sivalingam, E., 1976, "Spectrum of Trabecular Pigmentation in Open-Angle Glaucoma: A Clinicopathologic Study," Trans. Am. Acad. Ophthalmol. Otolaryngol., **81**, pp. 258–276.
[21] Kuchle, M., Christian, Y. M., Nguyen, N. X., Martus, N., 1998, "Quantification of Aqueous Melanin Granules in Primary Pigment Dispersion Syndrome," Am. J. Ophthalmol., **126**, pp. 425–431.
[22] Bergenske, P. D., 1980, "Krukenberg's Spindle and Contact Lens-Induced Edema," Am. J. Optom. Physiol. Opt., **57**(12), pp. 932–935.
[23] Epstein, D. L., Freddo, T. F., Anderson, P. J., Patterson, M. M., and Chu, S. B., 1986, "Experimental Obstruction to Aqueous Outflow by Pigment Particles in Living Monkeys," Invest. Ophthalmol. Visual Sci., **27**, pp. 387–395.
[24] Gray, H., 1918, "Angiology (The Blood)," *Anatomy of the Human Body*, Lewis, W. H., ed., Lea & Febiger, Philadelphia, http://www.bartleby.com/107/134.html
[25] Riley, H. D., "Krukenberg's Spindle," *V553 Anterior Segment Path Lecture Notes*, http://www.opt.indiana.edu/Riley/HomePage/V553_Path_Slide_Lecture/6Krukenberg's_Spindle.html
[26] Fitt, A., home page, pictures of eyes, Department of Mathematics, University of Southampton, United Kingdom, http://www.maths.soton.ac.uk/staff/Fitt/eyes.htm
[27] Wilson, F. M., 1980, "Traumatic Hyphema: Pathogenesis and Management," Ophthalmology, **87**, pp. 910–919.
[28] Crouch, E. R., and Crouch, E. R., 1999, "Management of Traumatic Hyphema: Therapeutic Options," J. Pediatr. Ophthalmol., **36**(5), pp. 238–250.
[29] Alessandro, L. P., Forster, D. J., and Rao, N. A., 1991, "Anterior Uveitis and Hypopyon," Am. J. Ophthalmol., **112**, pp. 317–321.
[30] Huillier, J. P., and Sbirlea, G. A., 2000, "Morphology of the Human Eye: Glaucoma Physiology and Laser Iridectomy," *Medical Applications of Computer Modeling: Cardiovascular and Ocular Systems*, Martonen, T. B., ed. WIT Press, United Kingdom.
[31] Yedder, R. B., and Bilgen, E., 1997, "Laminar Natural Convection in Inclined Enclosures Bounded by a Solid Wall," Heat Mass Transfer, **32**, pp. 455–462.
[32] Mallinson, G. D., and Davis, G. D. V., 1977, "Three-Dimensional Natural Convection in a Box: A Numerical Study," J. Fluid Mech., **83**(1), pp. 1–31.
[33] Ergun, S., 1952, "Fluid Flow Through Packed Columns," Chem. Eng. Prog., **48**(2), pp. 89–94.
[34] Haider, A., and Levenspiel, O., 1989, "Drag Coefficient and Terminal Velocity of Spherical and Nonspherical Particles," Powder Technol., **58**, pp. 63–70.
[35] Doormal, J. P., and Raithby, G. D., 1984, "Enhancements of the SIMPLE Method for Predicting Incompressible Fluid Flow," Numer. Heat Transfer, **7**, pp. 147–163.
[36] Lutzen-Drecoll, E., 1973, "Structural factors influencing outflow facility and its changeability under drugs," Invest. Ophthalmol., **12**, pp. 280–294.
[37] Ethier, C. R., Kamm, R. D., Palaszewski, B. A., Johnson, M. C., and Richardson, T. M., 1986, "Calculations of Flow Resistance in the Juxtacanalicular Meshwork," Invest. Ophthalmol. Visual Sci., **27**, pp. 1741–1750.
[38] Lai, W. W., Bhavnani, V. D., Tessler, H. H., and Edward, D. P., 1999, "Effect of Melanin on Traumatic Hyphema in Rabbits," Arch. Ophthalmol. (Chicago), **117**, 789–779.
[39] Kampik, S., Green, W. R., Quigley, H. A., and Pierce, L. H., 1981, "Scanning and Transmission Electron Microscopic Studies of Two Cases of Pigment Dispersion Syndrome," Am. J. Ophthalmol., **91**, 573–587.
[40] Komaromy, A. M., Brooks, D. E., Kallberg, M. E., Andrew, S. E., Ramsey, D. T., and Ramsey, C. C., 2000, "Hyphema. Part II. Diagnosis and Treatment," COO Rep., **22**(1), pp. 74–79.
[41] Lozada, G., Rosedale Vision Center, Kansas City, KS, www.rosedalevision.com/eyecare.htm
[42] Olsen, T. W., Sternberg, P., Martin, D. F., Capone, A., Lim, J. I., and Aaberg, T. M., 1996, "Postoperative Hypopyon after Intravitreal Bovine Thrombin for Macular Hole Surgery," Am. J. Ophthalmol., **121**(5), pp. 575–577.